

Article

Multiscale Investigation of Microcracks and Grain Boundary Wetting in Press-Hardened Galvanized 20MnB8 Steel

Martin Arndt ¹, Philipp Kürnsteiner ^{2,3,*} , Tia Truglas ², Jiri Duchoslav ⁴ , Kurt Hingerl ⁴, David Stifter ⁴, Christian Commenda ¹, Johannes Haslmayr ¹, Siegfried Kolnberger ¹, Josef Faderl ¹ and Heiko Groiss ² 

¹ Voestalpine Stahl GmbH, Voestalpine-Straße 3, 4020 Linz, Austria; martin.arndt@voestalpine.com (M.A.); siegfried.kolnberger@voestalpine.com (S.K.); josef.faderl@voestalpine.com (J.F.)

² Christian Doppler Laboratory for Nanoscale Phase Transformations, Center for Surface and Nanoanalytics (ZONA), Johannes Kepler University Linz, Altenberger Straße 69, 4040 Linz, Austria; heiko.groiss@jku.at (H.G.)

³ Department Microstructure Physics and Alloy Design, Max-Planck-Institut für Eisenforschung GmbH, Max-Planck-Straße 1, 40237 Düsseldorf, Germany

⁴ Center for Surface and Nanoanalytics (ZONA), Johannes Kepler University Linz, Altenberger Straße 69, 4040 Linz, Austria; jiri.duchoslav@jku.at (J.D.)

* Correspondence: philipp.kuernsteiner@jku.at

Abstract: Grain boundary wetting as a preliminary stage for zinc-induced grain boundary weakening and embrittlement in a Zn-coated press-hardened 20MnB8 steel was analyzed using electron backscatter diffraction, Auger electron spectroscopy, energy dispersive X-ray analysis, atom probe tomography and transmission electron microscopy. Microcracks at prior austenite grain boundaries were observed. Structures that developed after microcrack formation were identified: for example, Zn/Fe intermetallic phases with grain sizes smaller than 100 nm were present at the crack surfaces and the wedge-shaped crack tips. An electrolytically coated reference sample that underwent the same heat treatment as the press-hardened material but without the application of tensile stress was investigated in order to find the initial cause of the microcracks. On this sample, Zn, in the order of one atomic layer, was found along prior austenite grain boundaries several micrometers away from the actual Zn/Fe phases in the coating. The resulting grain boundary weakening with the Zn wetting of prior austenitic grain boundaries during austenitization and/or hot forming is a necessary precondition for microcrack formation.

Keywords: press-hardened galvanized steel; liquid metal embrittlement; prior austenite grain boundaries; grain boundary diffusion; microcracks; zinc–iron reaction



Citation: Arndt, M.; Kürnsteiner, P.; Truglas, T.; Duchoslav, J.; Hingerl, K.; Stifter, D.; Commenda, C.; Haslmayr, J.; Kolnberger, S.; Faderl, J.; et al. Multiscale Investigation of Microcracks and Grain Boundary Wetting in Press-Hardened Galvanized 20MnB8 Steel. *Metals* **2024**, *14*, 46. <https://doi.org/10.3390/met14010046>

Academic Editors: Dongsheng Qian and Feng Wang

Received: 25 October 2023

Revised: 30 November 2023

Accepted: 13 December 2023

Published: 29 December 2023



Copyright: © 2023 by the authors. Licensee MDPI, Basel, Switzerland. This article is an open access article distributed under the terms and conditions of the Creative Commons Attribution (CC BY) license (<https://creativecommons.org/licenses/by/4.0/>).

1. Introduction

Press-hardened ultra-high-strength steel (PHS) is the material of choice for structural components in lightweight automotive body technology to reduce vehicle weight and increase passenger safety [1]. In the press-hardening process, PHS blanks are heated up to temperatures above 870 °C and subsequently quenched and hardened. There are two variants of the press-hardening process, namely, the direct and the indirect processes. In the indirect process, preformed parts are heated up and quenched in a die. In the direct process, a flat blank is heated up, and forming as well as quenching is performed in one single step. The steel surface is protected by a zinc (Zn) coating from oxidation during the final annealing process, in which the former ferritic and bainitic structure transforms again into austenite (γ -Fe). During the subsequent quenching, the steel sheet is formed with hot stamping, which leads to a hard, martensitic structure. The hot-dip galvanized Zn coating not only prevents the steel from oxidation during annealing but also performs excellently as corrosion protection [2].

However, Zn coatings on steel combined with heat treatments also present a challenge. Zn can embrittle the steel, and macroscopic cracks can occur during the further processing

steps. Grain boundary (GB) weakening by Zn is supposed to be the underlying mechanism of this metal-induced embrittlement (MIE), which is therefore highly influenced by different alloy compositions and their resulting microstructures [3–6]. Already a monolayer or even a sub-monolayer of Zn at a GB has a strong impact on its strength [7]. The transport of Zn to the GBs can happen by solid-state diffusion (solid metal-induced embrittlement, SMIE) [8], by liquid Zn (liquid metal-induced embrittlement, LMIE), or even due to Zn vapor [9]. Since Zn liquifies at quite a low temperature of 420 °C, LMIE is the most prominent process that has been a topic for more than 100 years, and it is still the focus of recent research [10–23].

Potential counteractions to prevent MIE are the binding of Zn with pre-cooling in Fe-Zn phases such as the Γ -Fe₄Zn₉ phase with a melting point of $T_m = 782$ °C or binding Zn by oxygen [24–26] in ZnO ($T_m = 1975$ °C, see Table 1). MIE is well under control in the manufacturing process of PHS systems by making use of the above-described effects and measures described in the review article by Ling et al. [27]. For example, by adding elements like boron to the underlying steel grade, one can lower the conversion into softer microstructures. Thus, it is possible to use less constrained cooling curves. However, the models of the different MIE mechanisms are still under debate. Understanding these mechanisms is a crucial step for the further development of PHS technology and new Zn-coated ultra-high-strength steel grades in general. In recent works [12–17], steel samples were tensile stressed at high temperatures so that liquid Zn could flow into the newly appearing cracks and form intermetallic Zn-Fe phases afterward. However, we believe that the formation of these phases hides the view of the initial stages of embrittlement, where the first interaction between the liquid Zn and the base steel occurs. This can hinder a better understanding of the underlying mechanisms of embrittlement. Thus, the aim of this study is to focus on the first wetting of GBs with Zn in order to gain a better understanding of the processes involved in the initial stages of LME. We use samples that underwent a heat treatment similar to the temperature history of industrially manufactured samples but without the application of any mechanical stress. In this way, we can simulate possible failures in production and investigate the initial stages of grain boundary weakening.

Table 1. Possible phases at the surface of PHS steels.

Phase	Composition	Lattice Constant (Å)	Crystal System	Space Group	Space Group Number	Melting Temp. (°C)
Ferrite	Fe	a = 2.8710	Cubic	I m $\bar{3}$ m	229	-
Γ	Fe ₄ Zn ₉	a = 8.9820 [28]	Cubic	I $\bar{4}$ 3 m	217	782
Γ_1	Fe ₁₁ Zn ₄₀	a = 17.9630 [29]	Cubic	F $\bar{4}$ 3 m	216	-
δ	FeZn ₁₁	a = 12.7870 c = 57.2220 [30]	Hexagonal	P 63/m m c	194	670
ζ	FeZn ₁₃	a = 10.8618 b = 7.6080 c = 5.0610 $\beta = 100.542^\circ$ [31]	Monoclinic	C 1 2/m 1	12	530
Zinc	Zn	a = 2.6640 b = 4.9469	Hexagonal	P 63/m m c	194	420
Zincite	ZnO	a = 3.2489 b = 5.2049	Hexagonal	P 63/m m c	186	1975

2. Experimental Details

2.1. Material and Sample Processing

For this study, galvanized boron steel (20MnB8 + GA90/90) was used, which is distributed by Voestalpine Stahl GmbH under the brand name phs-directform 1500. The alloy elements in the steel are C 0.2 wt%, Si 0.2 wt%, Mn 2 wt%, and B 30 ppm. The thickness of the steel sheets is approximately 1.5 mm. The steel was hot-dip galvanized in

a Zn bath at 460 °C containing 0.15 wt% Al and galvanized with a final layer thickness of about 12.5 µm. A Fe-Zn phase diagram adapted for boron steel can be found in Ref. [32] for 22MnB5. This phase diagram also represents the used 20MnB8 steel better than the standard Fe-Zn phase diagram.

To simulate MIE cracks, we used a laboratory-scale process that simulates realistic production conditions and provokes microcracking. Specifically, we deformed sample strips with sizes around 20 × 120 mm² in a die [26]. First, the strip of the Zn-coated base material was heated in a radiation furnace to 900 °C and annealed for 45 s at a temperature above 870 °C. The sample was subsequently cooled in air to 600 °C and finally bent in the tool reaching a temperature of 100 °C, as presented in the thermal processing curve in Figure 1a. This precooling step down to 600 °C corresponds to the industrial process preventing so-called first-order LMIE due to liquid Zn. Cracks appeared at the stretched coating-steel surface, as indicated in Figure 1b, and continued into the base steel, as depicted in the SEM cross-section image in Figure 1c.

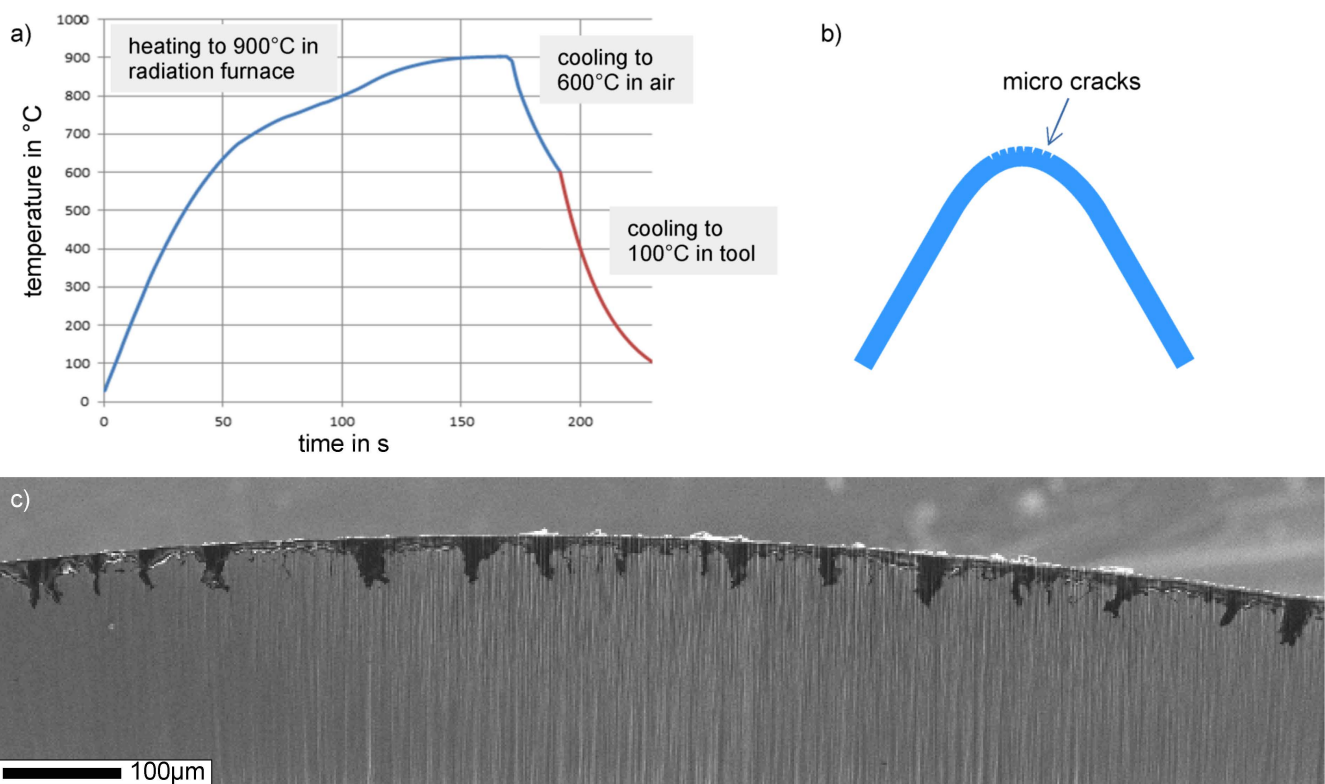


Figure 1. (a) Thermal processing curve of a PHS sample (hot-dip galvanized 20MnB8) in order to simulate realistic production conditions and provoke microcracking, (b) sketch of the deformed sample with microcracks at the stretched surface, and (c) secondary electron image of micro-cracks (filled with epoxy resin to avoid redeposition during sample preparation) at the bent surface in a cross-section view.

The interaction between the Zn-coating and the base steel was analyzed on a second set of samples. The large interface roughness between the base steel and the Zn coating of the steel substrate offered some challenges regarding the preparation of samples for transmission electron microscopy (TEM) with focused ion beam (FIB) cutting. In addition, the large Zn coating thickness and ferrite grain sizes compared with the final specimen size achievable with FIB milling made a targeted preparation complex. To avoid these challenges, we fabricated well-defined test samples, which minimized the impact of production artifacts on the industrial sample surfaces (for instance, laps or double skin from rolling). For that purpose, we used a similar galvanized 20MnB8 steel to ensure the same microstructure and removed the Zn coating with polishing to obtain a clean steel surface.

Subsequently, a new Zn layer was deposited on the steel sample with electroplating, which creates a well-defined steel substrate-Zn interface. This strip was then annealed in the same way as the first type of samples for 45 s above 870 °C and remained undeformed. It should be noted that this substrate-Zn interface does not contain a Fe₂Al₅ inhibition layer. Furthermore, such an inhibition layer is not present in the hot-dip galvanized samples since any present inhibition layer is dissolved quite early in the galvannealing process.

2.2. Analytical Tools and Measurement Conditions

Cross sections were analyzed in a Zeiss Supra 35 field emission scanning electron microscope (SEM) (Carl Zeiss AG, Oberkochen, Germany) with an X-Max^N 80 mm² energy dispersive X-ray detector (EDX) and a NordlysNano electron backscatter diffraction (EBSD) detector. Both detectors are from Oxford Instruments, Oxford, England and can be used simultaneously. The cross sections were produced with Argon ion sputtering in an ion beam milling system Leica TIC 3X (Leica, Wetzlar, Germany) at −100 °C with an ion beam energy of 8 keV. The sample surface was protected from re-deposition in the sputter chamber with an ink layer of a black felt tip pen and copper tape.

The crystal structures and lattice parameters were identified with X-ray diffraction (XRD) (X'Pert PRO MPD, Malvern Panalytical, Kassel, Germany and Rietveld refined, see Table 1 for the literature values used). The found phases were transferred into the Aztec[®] program (version 4.1. SP1) and were used as a reference list for phase identification during EBSD mapping. The phases with the highest volume fraction, namely, bcc-iron (ferrite), Γ - and Γ_1 -phases are cubic and can hardly be distinguished. Also, the hexagonal phases Zn, ZnO, and δ are too similar to be distinguishable with EBSD. Additionally, the Γ_1 lattice constant is exactly the double of the Γ phase, which also complicates the identification of these phases with XRD.

Cross-sections were also analyzed with Auger electron spectroscopy (AES) in a JAMP 9500F from JEOL, Tokyo, Japan. The instrument is equipped with a fracture stage that is flange-mounted to the main chamber. This allows breaking samples after cooling with liquid nitrogen and measuring the fractured surfaces without leaving the ultra-high vacuum (base pressure 5×10^{-8} Pa). All Auger spectra were taken in constant retard ratio mode (CRR) with an energy resolution of about $\Delta E/E = 0.5\%$. The primary electrons were accelerated to 30 keV at currents between 10 and 20 nA. Auger element mappings were conducted in constant analyzer energy mode (CAE). The depth information was about 6 nm, and the lateral resolution was 10 nm. Although the instrument is equipped with an Ar ion sputter gun, the sample surfaces were not sputtered in order to keep the original preparation state.

Transmission electron microscopy (TEM) was performed in a JEOL JEM-2200FS instrument (JEOL, Tokyo, Japan) equipped with an Oxford Instruments X-Max^N 80T EDX-detector (Oxford Instruments, Oxford, England), at 200 keV primary beam energy. The instrument was operated in scanning TEM mode using a bright field (BF) and a high angle annular dark field (HAADF) detector. Sample preparation for TEM was conducted by FIB cutting in a Zeiss 1540 XB SEM (Carl Zeiss AG, Oberkochen, Germany). The surface of the sample with microcracks was covered prior to FIB cutting with epoxy resin M-Bond 610 from Vishay Micro-Measurements, Toronto, ON, Canada in order to fill the cracks and potential pores to avoid re-deposition of the sputtered material.

Atom probe tomography (APT) was used to obtain a detailed chemical composition of the Zn coating and the base steel. Additionally, segregation at defects in the base steel was investigated using this method. FIB milling with an FEI Helios Nanolab 600i (Thermo Fisher Scientific, Waltham, MA, USA) was used to prepare specimens for APT. Specimens were prepared using the standard liftout procedure. More details about the liftout procedure are given in the Supplementary Materials section (see Figures S1–S3). APT tips were sharpened at 30 keV with annular milling. A final low-energy milling step at 5 keV for 1 min was applied to reduce Ga contamination at the tip surface. APT experiments were conducted in a Cameca LEAP 5000X HR (Thermo Fisher Scientific, Waltham, MA, USA) and a LEAP

5000 XS (Thermo Fisher Scientific, Waltham, MA, USA), both operated in laser mode. Pulse frequencies of 333–625 kHz and 125–333 kHz were used together with detection rates of 1.5–3% and 1.3–1.7% for the XS and the HR device, respectively. Temperatures between 40 K and 60 K and laser energies between 35 pJ and 60 pJ were used for both devices. In order to cross-check the composition obtained with APT in laser mode, two additional measurements were performed in voltage mode at a temperature of 50 K, a detection rate of 1.2%, a pulse fraction of 15%, and a pulse frequency of 250 kHz. The compositions were found to be the same with both operation modes of the atom probe instrument. The commercial software IVAS (version 3.8.4) was used to reconstruct the APT specimens.

3. Results

3.1. Metal-Induced Embrittlement Cracks

The first analyzed structure was taken from the hot-dip galvanized PHS strip, which was deformed during cooling. The cross-section of the sample was investigated using EBSD and EDX, with the results of this measurement presented in Figure 2. The general structure of the coating system is indicated in the band contrast (BC) image of Figure 2a. Starting with the base steel, it is (i) martensite, (ii) Zn-saturated ferrite (α -Fe(Zn)), (iii) Zn/Fe-phases (mostly Γ -phase), and (iv) ZnO (zincite, if crystalline). In the band slope (BS) image (Figure 2b), martensite can be clearly distinguished from ferrite. A few ferrite islands can be observed, but the microstructure is mainly martensitic. The dark regions correspond to martensite due to the high density of sub-grain boundaries and dislocations. Figure 2c shows the EBSD phase map, in which the three phases bcc-Fe (martensite and α -Fe(Zn)), Γ -phase, and ZnO are shown. Close to the α -Fe(Zn), the Γ -phase was partially incorrectly identified as the bcc-iron phase because the crystal structures of both phases are very similar. Another feature that is well-visible as dark areas in the Γ -phase region is the pores reaching from the surface far into the Γ -phase. Figure 2d combines the BC with the EDX Zn K_{α} and Fe K_{α} maps. A sharp boundary is visible in the α -Fe(Zn) grains that touch the bulk martensite, where the Zn concentration decreases from about 30 wt% to approximately 0 wt% close to the martensite. This leads to a small region of Zn-free ferrite (α -Fe) grain sections separating the Zn in the α -Fe(Zn) grains from the bulk martensite. Similar findings of additional phase separation of the α -Fe(Zn) from the bulk martensite at the interface region were found in related Zn-coated steel systems [18,33], as discussed further below. The measured Zn concentration in the Zn-rich part of the α -Fe(Zn) is around 30 wt%, and only traces of the alloy elements Al, Mn, Si, and Cr can be found. In the underlying martensite, the alloy concentrations of the steel are detected with only a quite low signal (<0.2 wt%) of Zn. No extended Zn-phases are observed in the crack in the martensite region.

The surrounding area of a crack tip (see Figure 3) was analyzed with the same techniques as the survey mapping but at a higher magnification. The fine martensitic structure around the crack can be seen in Figure 3a. The Zn K_{α} EDX map shown in Figure 3b reveals that the crack surface is covered with Zn, which is presumably due to the fact that liquid Zn or Zn vapor was present after the crack formed. Furthermore, the Zn concentration at the two marked crack tips is higher compared with the remaining cracked surface. Figure 3a also shows some misorientation angles from opposite sides of the crack tips. The austenite grains that are present at higher temperatures transform into martensite during rapid cooling. The transformation follows the Kurdjumov–Sachs mechanism, which predicts the orientation relation of martensite grains to their prior austenite grain. No possible grain orientation between 21.06° and 47.11° exists according to this relation [34,35] for martensite grains originating from the same austenite grain. Thus, martensite grains exhibiting an angle between these values have to originate from different austenite grains. Indeed, the measured misorientation angles of grains from opposite sides of the crack tip between 24° and 37° indicate cracking along prior austenite grain boundaries (PAGBs). This is in good agreement with the recent results obtained by Takashi et al. [11] and Bhattacharya et al. [36], who also found cracking along PAGBs.

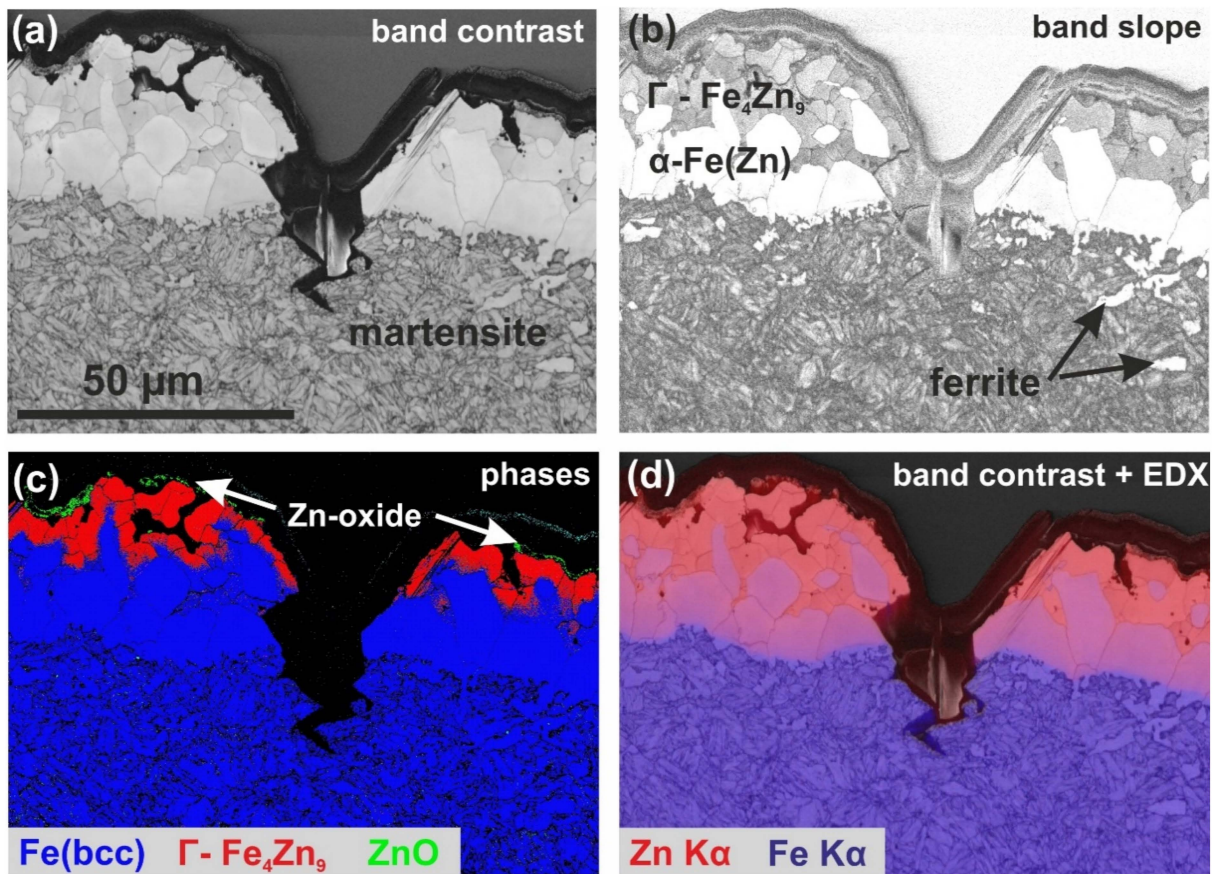


Figure 2. The cross-section of a crack in the hot-dip galvanized, deformed sample: (a) EBSD band contrast, (b) band slope contrast, (c) overlay of ferrite, Γ -phase, and zincite, and (d) an overlay of band contrast and the EDX Zn K_{α} and Fe K_{α} signals.

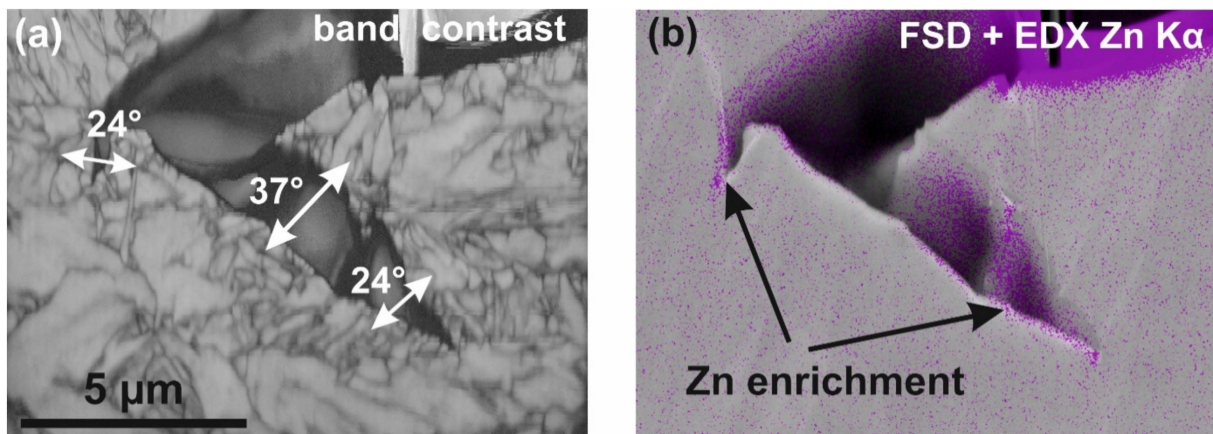


Figure 3. (a) EBSD band contrast mapping of the crack tip and (b) a front scatter detector image overlaid with an EDX Zn K_{α} signal.

To obtain a deeper insight into the composition of the crack tip, AES measurements were performed (see Figure 4). Since EBSD mapping leads to carbon contamination in the map area and AES is extremely surface sensitive, another crack similar to that shown in Figure 3 was chosen for AES measurements. Figure 4a shows the secondary electron image of a similar crack tip on the same sample, where six Auger spectra (Figure 4d) were taken at the marked positions. Oxides and carbon contamination form rapidly during sample handling after preparation in an ambient atmosphere. Therefore, traces of C and O

are present in all spectra, but these are not further discussed under the assumption that they do not affect the distribution of the other elements. On the contrary, oxidation can even help to reduce the mobility of Zn (by incorporating Zn into the Zn oxide crystal) and freeze the original Zn distribution. The only two other elements that can be observed in the spectra are Fe and Zn. First, this is proof that the sample preparation is suitable because no re-deposition of elements like Cr, Ni, Cu, or Al from the stainless steel walls of the sputter chamber or Al- and Cu-tapes used to protect the sample are present. Fe is found in all spectra, while Zn only occurs at the crack surface (spectra 4–6) and the crack tip (spectrum 1). No Zn can be found in spectra 2 and 3, which indicates the absence of significant Zn bulk diffusion. The Zn concentrations in spectra 4–6 are comparably low, and deviations between these three spectra can be explained by the different angles of the surfaces facing the detector. The highest Zn concentration is found in spectrum 1 at the crack tip. A quantification of this spectrum gives the following concentrations in at%: C 45.5, O 33.8, Fe 14.3, and Zn 6.4. The Fe/Zn ratio of approximately 7/3 indicates that the material at this position was a Zn-Fe phase with 30 at% Zn before oxidation. Furthermore, the Auger mapping (Figure 4b,c) using the Zn_{LMM} signal reveals a triangular, pointy shape of the Zn-enriched area at the crack tip along the crack direction.

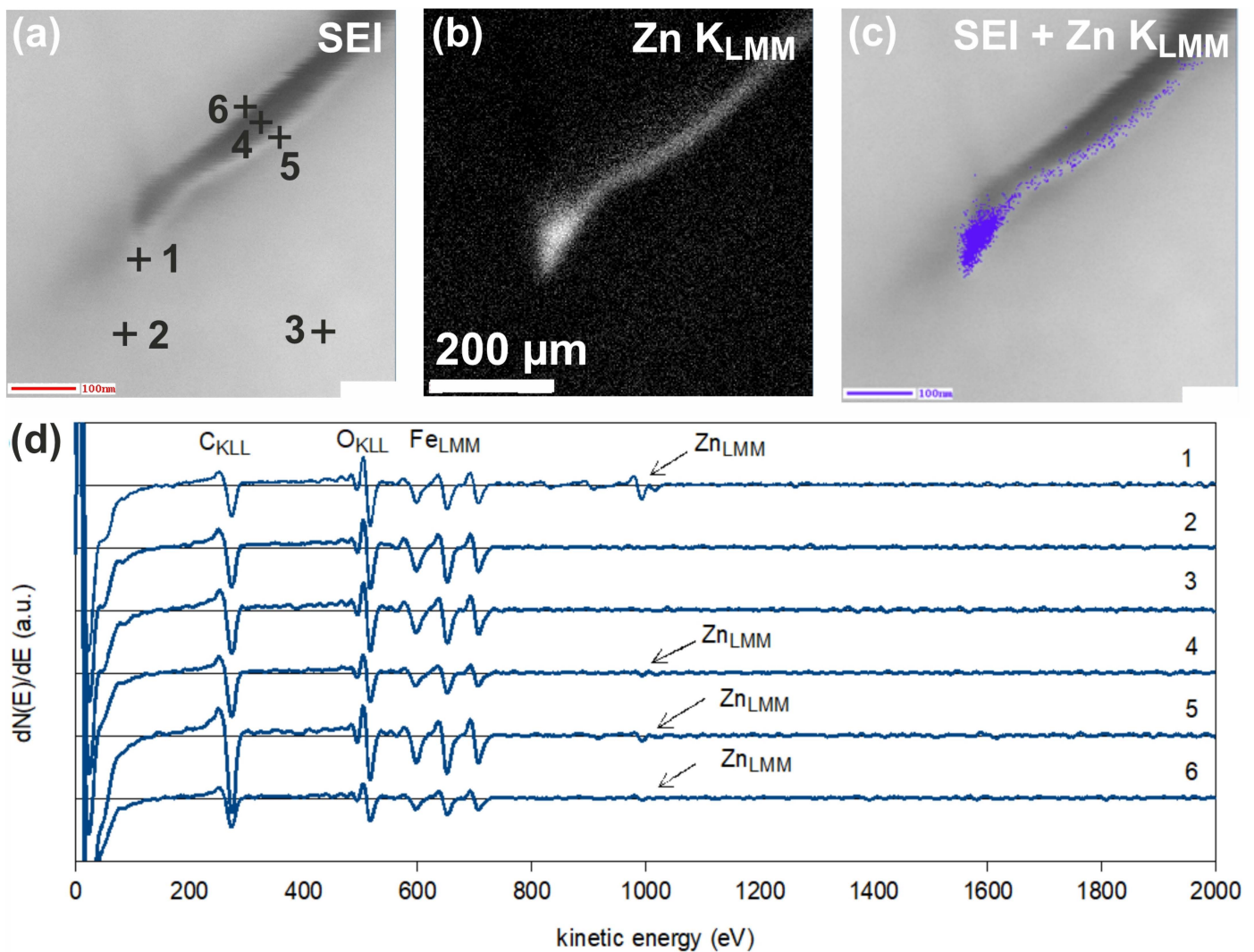


Figure 4. (a) Secondary electron image of a crack tip in the hot-dip galvanized, deformed sample prepared with cross-section argon sputtering, (b) the corresponding Zn_{LMM} Auger mapping, (c) the overlay of both, and (d) the Auger derivative spectra. The surface of the crack is covered with Zn. The crack tip was an α -Fe(Zn) wedge smaller than 100 nm before oxidation.

An additional crack in the analyzed sample was prepared as an FIB lamella for STEM investigations. Figure 5a shows the HAADF image of the analyzed area. The dark area in the top right corner is the crack, which is filled with epoxy resin to avoid re-deposition onto the surface during FIB cutting. The vertical stripes are due to thickness variations in the lamella, a well-known FIB-preparation artifact called the curtaining effect, resulting from the inhomogeneous surface and grain structure of the complex steel sample. The lamella was subsequently analyzed with EDX. Figure 5b shows the Zn K_{α} map, where three different aspects are evident. First, the map confirms the observation made in Figure 4 that Zn is present at the crack surface. Second, it also shows a triangular-shaped Zn phase at the crack tip similar to Figure 4b,c. Third, a new finding is that Zn penetrates further into the steel at the tip of the Zn wedge. The position of the Zn at the edge of the crack is confirmed in Figure 5c, which displays the overlay of the HAADF STEM image with the Zn K_{α} map. Additionally, a further structure found in this EDX measurement is displayed, which shows small precipitates containing the alloying element titanium.

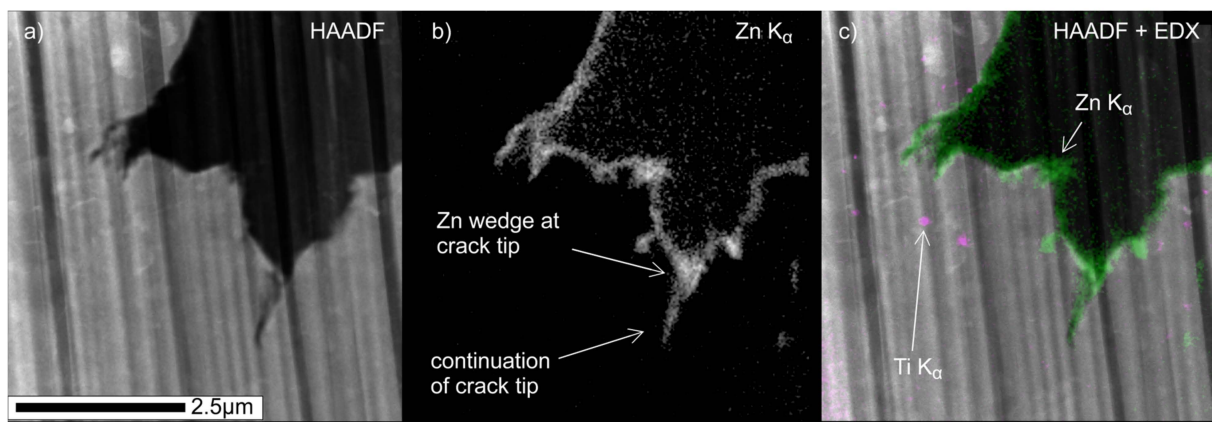


Figure 5. (a) HAADF STEM image of a crack tip in the hot-dip galvanized, deformed sample. (b) Zn EDX mapping made with TEM and (c) and overlay of both. The Zn distribution shows that the surface of the crack is covered by Zn. It also shows the Zn wedge at the crack tip. At the tip of the Zn wedge, the Zn profile extends into the base steel.

3.2. Interaction between Zn and the Undeformed Base Steel

Two important questions are how far Zn penetrates into the base steel before cracking and whether the penetration of Zn into the GBs requires bending of the sample and an external force during cooling. For this purpose, the second experiment with the Zn-electroplated, undeformed base material was performed, which was annealed in the same way as the MIE-affected sample.

The cross-section of the sample was polished and subsequently measured with EBSD and EDX similar to the first deformed sample. Figure 6a shows the band contrast image of a surface cross-section. Overlays of this band contrast with EDX data and EBSD phases are shown in Figure 6b–d. As expected, and proving our experimental concept, we found similar structures as in the bent sample shown in Figure 2. The bulk consists of martensite. The next layer is composed of α -Fe(Zn). Here again, a sharp internal boundary occurs where the Zn concentration increases from approximately 0 to 30 wt% leading to a thin Zn-free region within the α -Fe grains located at the α -Fe(Zn)/martensite interface. This Zn-free ferrite region is an almost continuous layer across the entire interface, interrupted only by some regions where the Zn-containing α -Fe(Zn) grains touch the martensitic base steel directly (see Figure 6 and Figure S2 in the Supplementary Materials section). The next layer consists of α -Fe(Zn) surrounded by Zn/Fe-phases (Γ - and δ -phase). The top layer is a continuous crystalline ZnO film with large pores beneath. This ZnO layer is thicker for the unbent sample in contrast to the sparse occurrence of ZnO on top of the bent sample. The reason is that the Zn layer of the bent sample is created with hot-dip galvanizing and galvannealing, in which the liquid Zn bath contains approximately 0.15 wt% Al. This leads

to an additional Al_2O_3 layer on top of the coating, which reduces Zn oxidation [37]. This missing Al_2O_3 layer of the electroplated sample displayed in Figure 6 leads to the formation of the thicker ZnO layer. Within the sensitivity of the combined EDX/EBSD measurement, no Zn is detected below the internal α -Fe(Zn) zinc boundary (see Figure 6 and Figure S2 in the Supplementary Materials Section).

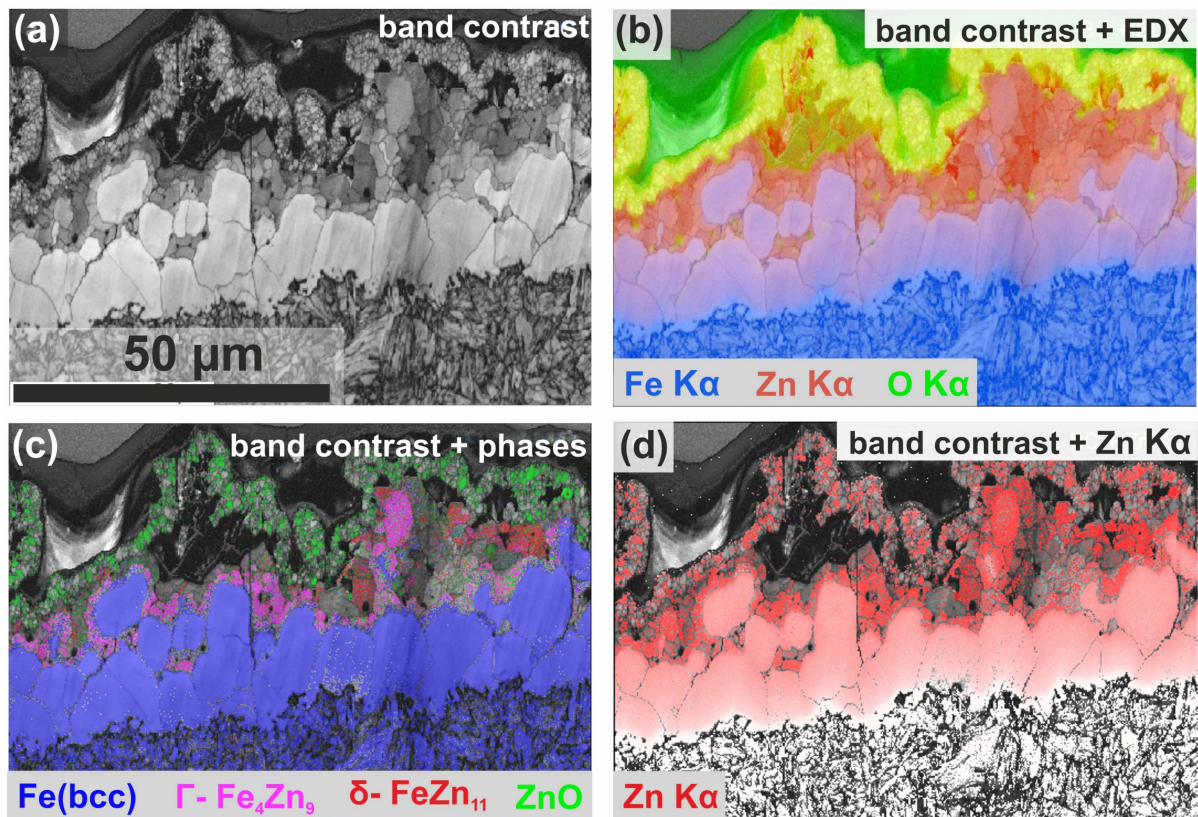


Figure 6. A cross-section of an electrogalvanized, undeformed sample: (a) EBSD band contrast, (b) overlay of band contrast with EDX Zn $K\alpha$, O $K\alpha$, and Fe $K\alpha$ signals, (c) overlay of band contrast with ferrite, Γ -phase, δ -phase, and zincite, and (d) overlay of band contrast with the EDX Zn $K\alpha$ signal.

To obtain a detailed elemental composition, APT measurements were performed. As explained in more detail in the Supplementary Materials section (see Figures S1–S3), multiple APT tips were measured along an approximately 10 μm long so-called liftout. In this way, we generated the composition profile from the Γ -phase and α -Fe(Zn) to the martensitic base steel shown in Figure 7. The composition of the Γ -phase is 31.9 at% Fe, 68.1 at% Zn, and a small amount of 0.033 at% Mn, which is very close to the stoichiometric composition of Fe_4Zn_9 (i.e., 69 at% Zn). A clear gradient in Zn composition with decreasing Zn content toward the base steel is present in the region of the α -Fe(Zn) phase. The Zn composition at the exact interface to martensite cannot be determined here since the composition profile consists of discrete APT measurement points being approximately 2 μm apart. The graph shows differently steep increasing concentrations of Si, Mn, Al, and Cr as well as C toward the base steel. The exact compositions of each APT measurement can be found in Table S1 in the Supplementary Materials section. The martensitic base steel exhibits a composition of approximately 0.4 at% Si, 1 at% Mn, 0.03–0.048 at% Al, 0.18 at% Cr, and 1.45–1.67 at% C. The Zn composition is found to be extremely low at only 0.002–0.003 at% (i.e., 20–30 ppm). The C content is higher than the nominal composition of 1 at%, which could be an enrichment in C during the α -Fe(Zn) formation on the steel base side due to a low solubility of the formed phase. Other reasons could be local variations in C concentration as well as C contaminations during any of the preparation steps.

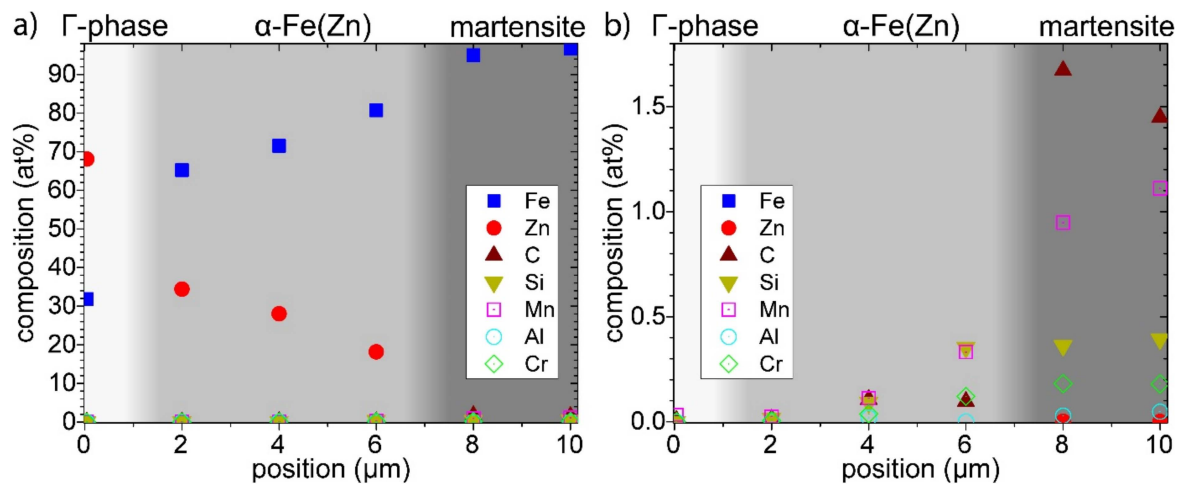


Figure 7. Elemental compositions determined with APT at the electrogalvanized, undeformed sample: (a) the chemical composition of the Zn coating system and the base steel, ranging from the Γ -phase over the α -Fe(Zn) to the martensitic base steel (left to right). Each set of data points at the different positions represents an individual APT measurement. More details can be found in the Supplementary Materials (Figures S1–S3). (b) A magnified view of the low-concentration regime from 0 to 1.8 at%.

If the samples contain PAGBs weakened by Zn, they should open up preferentially during fracture [7]. Thus, we looked for the presence of Zn in the martensite base steel below the α -Fe(Zn) on fractured surfaces prepared with a fracture stage, which is attached to the Auger instrument. This allows us to analyze the fractured surface in situ with Auger electron spectroscopy without leaving the ultra-high vacuum. In this way, we can avoid any surface contamination or oxidation. Figure 8a shows such a fractured surface, where six Auger spectra measurement positions are marked. The image is also overlaid with an EDX mapping of the fractured surface that was performed after the Auger measurements. The EDX map reveals the interface between α -Fe(Zn) and martensite. The positions of the measured point spectra are all positioned beneath this interface. The only small regions with Zn in the martensite are fracture splinters, which were avoided for the spectra measurements. Figure 8b shows the Auger spectra, which were taken around the Zn energy range. A significant Zn_{LMM} peak was found in spectra 1–4, which means that Zn is still present on the fractured surface 25 μ m away from the α -Fe(Zn)/martensite interface in the martensitic steel region. The Zn concentration of spectrum 4 was quantified by taking a complete spectrum from 0 to 2000 eV (not shown here), which resulted in a Zn concentration of approximately 0.6 at% Zn. This Zn concentration found with AES on the fracture surface is much higher than the Zn content of the martensitic matrix determined with APT to be 0.002 at%. These results show that the fracture surface exhibits a local enrichment in Zn, i.e., a Zn-enriched GB that was weakened and therefore opened up preferentially upon fracture as intended with this experiment. The Zn concentration determined with AES is much lower than the Zn concentrations measured at ferrite grain boundaries by Allegra et al. [38] after long-time diffusion experiments. However, if the information depth of AES is estimated to be a few nm, then the AES result of 0.6 at% Zn can be an amount of a Zn monolayer or a comparably thick Zn-Fe phase at the fractured surface. This is the same order of magnitude of the unwanted element as in the studies of Luo et al. [39] on a simpler system, in which a bilayer of Bi was found to be responsible for LMIE of austenite grain boundaries in Ni. For SEM-EDX, it is impossible to determine such low Zn concentrations at surfaces because the information depth is several hundreds of nm. Indeed, no Zn was detected (in addition to the splinters that formed during the in situ fracture in the AES chamber) in the martensite regions with SEM-EDX on the fractured surface.

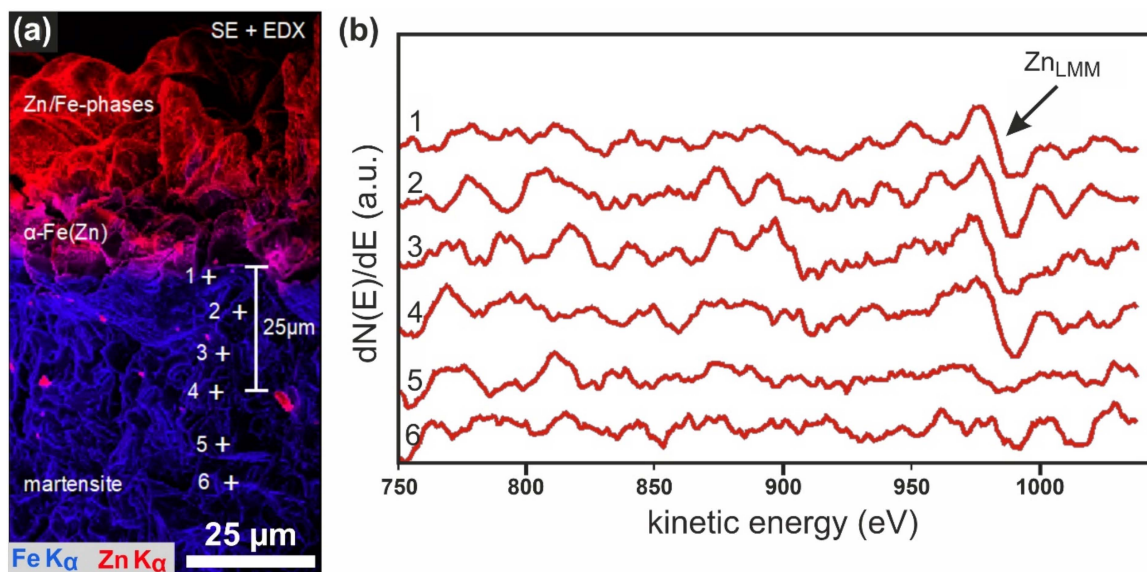


Figure 8. Six Auger measurement positions at a fractured surface of the electrogalvanized, undeformed sample prepared in a UHV fracture stage mounted to the Auger instrument. (a) An overlay of the secondary electron image with the EDX Zn K_{α} and Fe K_{α} mappings. The corresponding differentiated Auger spectra are displayed in (b). One can see that Zn can be detected down to 25 μm below the Zn boundary in the α -Fe(Zn) layer. Subsequently, the area was EDX-mapped in an SEM to ensure the correct Auger measurement positions below the α -Fe(Zn).

These low amounts of Zn make it quite difficult to identify a Zn-wetted GB and prepare it for further measurements like APT, which would be perfectly suited to determine such small concentrations. For the liftouts, we target grain boundaries in the α -Fe(Zn) that continued straight into the martensite and where no Zn-free ferrite section was present. Unfortunately, we could not unambiguously identify a PAGB in the APT measurements, for details see the Supplementary Materials section (see Figure S4). However, we successfully prepared a TEM lamella from the undeformed electroplated sample in order to perform an EDX-STEM analysis with higher sensitivity compared with SEM-EDX. Figure 9a shows a bright field STEM image with the martensitic microstructure of the base steel at the bottom and the α -Fe(Zn) layer (identifiable by a more homogeneous light gray color) at the top of the image. One can recognize two GBs enclosing a group of martensite grains, which, according to our interpretation, represent a prior austenite grain. The GBs are marked with two EDX mapping areas and arrows pointing toward them. The GB displayed in Figure 9b was confirmed to be a PAGB with transmission Kikuchi diffraction. The misorientation between the two neighboring grains was measured to be approximately 5° , which is clearly between the two possible orientations according to Kurdjumov-Sachs: 0° and 10.53° [34,35]. The EDX-mappings were recorded over several hours in order to have sufficient counts for a reliable signal evaluation of elements with low concentration. Figure 9b exhibits a Zn enrichment along the PAGB deep into the martensite, where Zn penetrates into the base steel at least 3 μm . Following the PAGB, no Zn could be measured any more after a few μm . Either the coverage of the GB decreases far below the detection limit, or it is a geometrical effect. The PAGB plane could be oriented in such a way that it is not parallel to the e-beam anymore, which would lower the small signal to the noise level.

Interestingly, this specific PAGB, which is clearly Zn-covered, is directly touching the Zn-containing region of the α -Fe(Zn), i.e., no Zn-free ferrite is present. In this region, the Zn-free lower part of the α -Fe(Zn) is missing and replaced with a Zn-containing martensite grain on either side of the boundary (labeled Zn-rich martensite in Figure 9b). Another observation can be made in the EDX mapping of the second PAGB displayed in Figure 9c. At this PAGB, no Zn can be found and no diffusion of Zn along the PAGB is present; instead, a continuous layer of Zn-depleted ferrite separates the Zn-saturated part from

the martensite base material. In this region, the Zn concentration decreases abruptly from 30 wt% to approximately 0 wt% within the α -Fe(Zn) grain. This observation matches the results from SEM-EDX and EBSD seen in Figures 2 and 6. For comprehensiveness, the Ti signal is also shown in these maps, which is the second alloy element we found to have a distinct distribution and form different precipitates in the surrounding PAGBs. Figure 9d,e displays the corresponding Mn K_{α} signal. We found an increased Mn content in the surroundings of the Zn-wetted PAGB. In the region of the second, non-Zn-wetted PAGB, no Mn segregation correlated with the GB can be observed. At the same time, small regions with significantly increased Mn content are present. These Mn-enriched regions are presumably Mn-rich precipitates such as Mn-Cr-carbides present in the 20MnB8 steel, which partially dissolve during the annealing step above 870 °C. Additional measurements at different lamellae reveal similar results. We found in most cases at least one Zn-wetted grain boundary in about 10 μm large lamellae, but not all PAGBs were wetted. This supports our argument that only some specific PAGBs are Zn-covered.

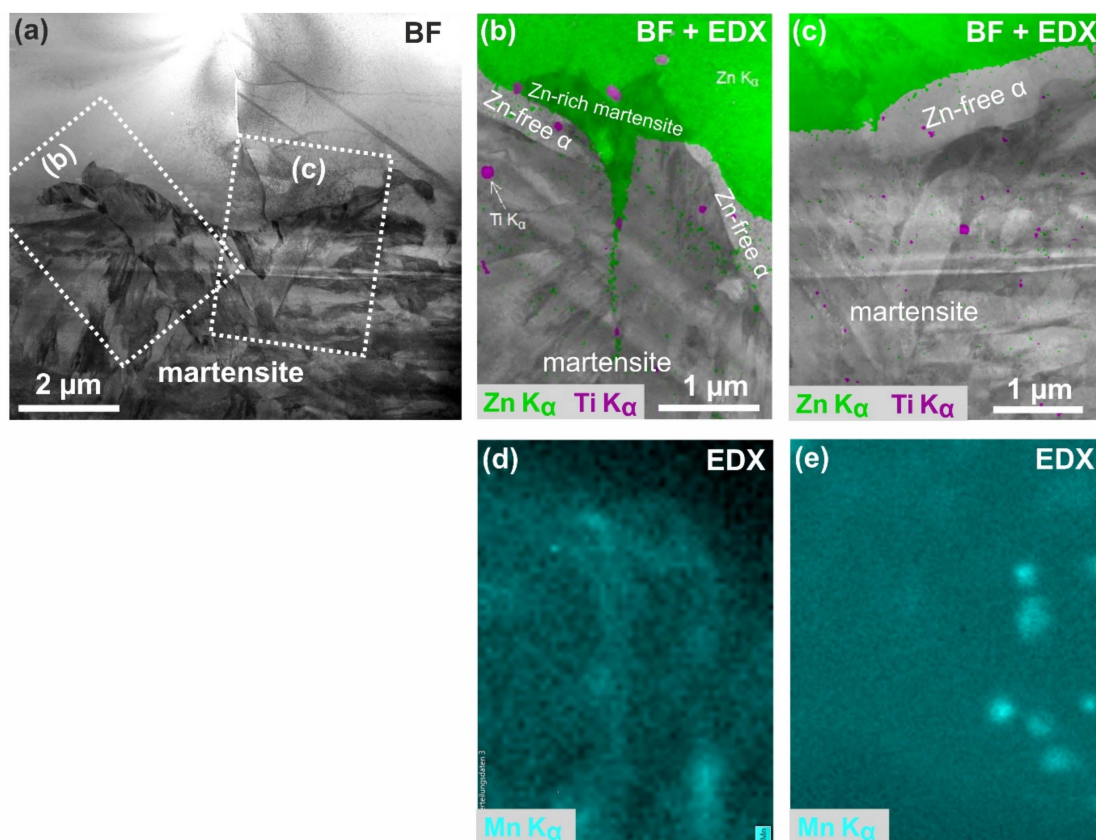


Figure 9. STEM measurements of the electrogalvanized, undeformed sample. (a) A STEM bright field image of a prior austenite grain in the martensite below the α -Fe(Zn). (b) The corresponding EDX signal of Zn K_{α} (green) and Ti K_{α} (purple) in an overlay with the bright field image, which shows the α -Fe(Zn) at the top. One can also see Zn along the prior austenite grain boundary. (c) The EDX mapping for the second neighboring austenite grain boundary, where no Zn wetting was observed. (d,e) The corresponding Mn K_{α} maps for the two PAGBs.

Different line scans were extracted from the mapping in Figure 9, as indicated in Figure 10a. Figure 10b shows a line profile starting in the martensite and crossing the Zn-free ferrite into the α -Fe(Zn). It can be clearly seen that the Zn signal decreases abruptly at the α -Fe(Zn)/Zn-free ferrite interface to almost zero. The decrease is even more abrupt than shown because the interface between the two phases is not perpendicular to the extracted line profile; thus, the signal is smeared out due to geometrical reasons. For comparison, Figure 10c is a line profile from the martensite through the Zn-containing martensite into

the α -Fe(Zn). Here, the Zn signal exhibits a small plateau of around 6 at% Zn at the position of the Zn-containing martensite, which fully fits a possible Zn solubility in austenite during annealing according to the phase diagram in ref. [32]. Both line profiles also display the Mn signal. Due to the general accuracy of EDX quantification, statements about the Mn are only possible to a limited extent. However, it seems that a small Mn increase is present at the martensite/Zn-free ferrite interface in Figure 10b, after that the Mn decreases continuously, which is also in accordance with the APT measurements (Figure 7b). In the phase diagram in ref. [32], on the other hand, it seems that the Mn content is slightly increased in the Zn-containing martensite, which was at the annealing stage, Zn-containing austenite. This points to the importance of Mn, in addition to C, in the stabilization of the different phases (e.g., austenite during quenching) at the coating–steel interface. We summed up all spectra from horizontal lines in the marked rectangle of Figure 10a to the quantitative line profile in Figure 10d. This line profile reveals the extremely low concentration of Zn along the grain boundary. The increased Mn content at the PAGB is also displayed. Due to noise and the Cu K_{β} (8.9 keV) peak, which overlaps Zn K_{α} , the statistical threshold for the quantification cannot be set so that the Zn concentration reaches zero far away from the GB. The increased Zn concentration at the GB is clearly visible and lies above the background. An estimation of the interaction volumes of AES and STEM, which are in the same order of magnitude, shows that the AES and STEM-EDX quantification values of 0.6 at% and 0.2 at% fit well together. This strongly indicates the presence of a small amount of Zn or Zn-Fe phases at PAGBs. Wetting with nm or sub-nm thick layers or more complicated GB complexions several μm deep along the PAGBs is conceivable.

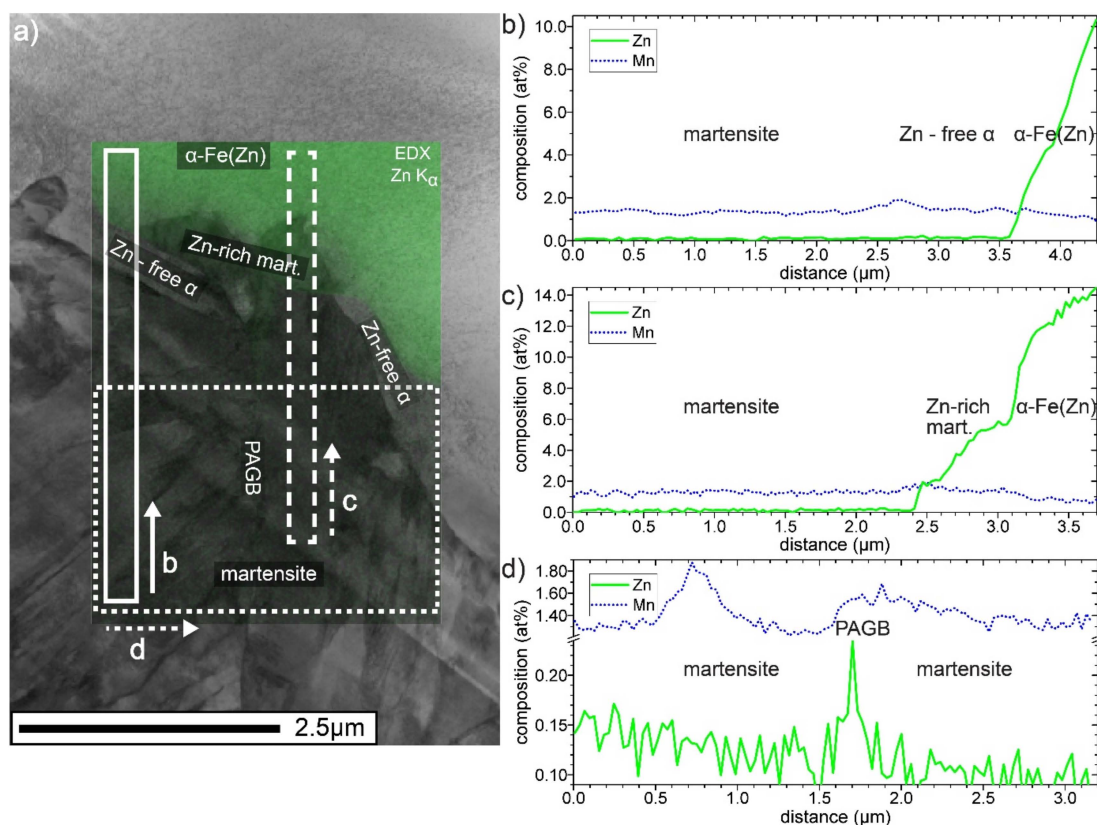


Figure 10. (a) The Zn K_{α} (green) mapping in an overlay with the bright field image of the wetted PAGB from the electrogalvanized, undeformed sample. (b) The quantitative line profile of the corresponding rectangular region in (a) starting at the arrow and crossing the Zn-free ferrite. (c) The corresponding line profile through the Zn-containing martensite. (d) A quantitative line profile obtained from the corresponding rectangular region in (a). Here, the line profile is generated from the sum spectra of all horizontal lines from left to right and displays the concentration changes cutting through the PAGB.

4. Discussion

Our investigations clearly prove the presence of small amounts of Zn at cracked surfaces and crack tips. Zn-induced crack formation at PAGBs is the reason for MIE in Zn-coated steel systems, and different models are discussed in the literature [13,15,18,32]. Strategies to avoid MIE in modern PHS systems use these facts and follow strategies to bind high mobile liquid Zn or Zn vapor with oxidation to hamper the transport of Zn to the crack tip or to generally allow the Zn to form stable phases by extended annealing holding times [16,17,26,32]. Investigations after crack formation highlight the Zn distribution and crack propagation but only allow a limited statement of whether the found Zn-phases were originally responsible for cracking or whether they were subsequently formed by Zn filling the crack. The question of how the initial stage of the embrittlement, i.e., the weakening of the GB, occurred, and thus, how the precondition of cracking is established, can hardly be answered on cracked samples. Thus, our undeformed samples allow a view of these first stages.

At typical austenitizing temperatures, in our case above 870 °C, one can conclude from the B-steel-Zn phase diagram [32] that the liquid Zn is enriched with Fe and that, at the same time, solid α -Fe(Zn) with up to 40 at% Zn can be formed at the contact region to the austenite (γ -Fe) matrix. Even if Zn can diffuse along austenite GBs leading to Zn-rich pockets, the α -Fe(Zn) formation is mainly governed by the liquid Zn γ -Fe reaction and solid-state bulk diffusion. The reason is that the Zn diffusing fast along GBs can also be dissolved relatively quickly in the bulk γ -Fe to form α -Fe(Zn). Depending on the increased austenite region in the B-steel-Zn phase diagram, the formation of Zn-rich austenite γ -Fe(Zn) is also possible [32,33]. After quenching, this can lead to a region of Zn-rich martensite between the α -Fe(Zn) and the bulk martensite, which was reported in related Zn-coated systems [18,33]. This Zn-rich martensite differs in its structure from bulk martensite. The different diffusion constants and solubilities of the alloy elements in Fe and Zn in the α -Fe(Zn) and the austenite (with later transforms to martensite) lead to locally quite different alloy element compositions with different transformation behavior compared with the bulk region. The work of Järvinen et al. [33] shows that the formation of this Zn-rich martensite layer strongly depends on the C content of the steel grade. An increased C content in the steel leads to a more pronounced Zn-rich martensite layer.

The 20MnB8 steel differs from the steels in Ref. [33] by a lower C and a higher Mn concentration. Thus, it is probable that this compositional difference and thermal processing parameters lead to a small region attached to the α -Fe(Zn) that is free of Zn and can transform into the Zn-free ferrite described in the results section. In detail, the higher diffusion rates of the carbon compared with the Fe, Zn, Mn, and the other alloy elements lead to a C-depleted region near the α -Fe(Zn), which can undergo transformation into ferrite instead of martensite. Figure 7 clearly shows the different behavior of the individual alloy element concentrations along the Zn-Fe reaction zone. The concentration of the alloy elements in the martensitic region at positions 8 and 10 in Figure 7 is around 1.5 at% C, 1 at% Mn, 0.4 at% Si, and 0.2 at% Cr. In the α -Fe(Zn) at position 6, the C and Mn decrease drastically to approximately 0.1 and 0.33 at%, whereas the Si and Cr change only slightly. In our system, this behavior results in the Zn-containing α -Fe(Zn) and the bulk martensite being well separated by a continuous layer of Zn-free ferrite almost everywhere, as can be seen in Figure 9c.

The APT measurements showed that the Zn composition in the martensitic matrix is extremely low, on the order of 0.002 at%. In addition, at defects such as dislocations as well as at random grain boundaries, no Zn segregation was found. It seems that not all but only some specific PAGBs are significantly enriched and therefore weakened by Zn. Such PAGBs were identified in our AES and STEM measurements. A deep in-diffusion of Zn along an austenite GB (at high temperatures, transforms to martensite when quenched) from the α -Fe(Zn) into the bulk can only take place if the Zn-containing phase or liquid Zn is in direct contact with a suitable austenite GB.

At this point, we should discuss what an austenite GB suitable for deep in-diffusion of Zn could look like. Typically, the solubility of Zn in austenite is quite low and Zn immediately forms α -Fe(Zn). Thus, one could expect that diffusion deep inside the base steel is unlikely to occur due to this reaction with the surrounding matrix. However, another case could be that Zn-rich austenite is stable and the α -Fe(Zn) formation does not take place. In this case, still, a limited solubility (strongly dependent on the exact alloy element concentrations) of Zn in the austenite and a small bulk diffusion will be present, leading to a deeper diffusion of Zn along the GB compared with the case with α -Fe(Zn) formation. C and Mn are both well-known austenite-stabilizing elements. Indeed, we find Mn enrichments at the position of the wetted PAGB (Figure 9d), which we assume to be the reason for a suppressed α -Fe(Zn) formation. This additionally implies that the austenite to Zn-free-ferrite formation cannot be present in these specific regions. The PAGB shown in Figures 9b and 10 is an example of this behavior, where Zn penetrates several μm into the base steel. At this specific PAGB, the Zn-free ferrite layer is replaced with a region of Zn-rich martensite surrounding the PAGB. The Zn-rich martensite (originated from Zn-rich austenite) with approximately 6 at% Zn directly touches the α -Fe(Zn) phase. We see at this position a well-visible indication of an increased Mn content in the surroundings of the Zn-modified PAGB (Figure 10d). Unfortunately, no statement can be made on the C distribution with STEM-EDX measurements.

Our results provide a strong hint that the exact local composition (e.g., enrichments or depletions in the alloy elements C, Mn, and Si) at the interface region and the austenite GBs strongly influences the Zn-Fe reaction and the ferrite and martensite formation. This can lead to arrangements in which Zn-containing phases are in direct contact with wettable austenite GBs above the austenitizing temperature, where the Zn-Fe reaction is delayed or suppressed. Generally, we would expect that a Zn-enriched GB at austenitization temperature later leads to a Zn-enriched PAGB. The AES measurements at fractured surfaces of the electrogalvanized, undeformed sample prove that the Zn penetration depth along PAGBs can reach 25 μm . Our experiments show that the actual Zn concentrations are very low, in the order of a monolayer or below, so that it is not possible to speak of bulk phases like α -Fe(Zn) or α' -Fe(Zn), which leads in some LMIE models to the cracking of the GBs. Zn-wetted PAGBs are weakened already by these low amounts of Zn. During the forming of the tool, these weak points can rip open and be the starting points of the macroscopic MIE cracks. After the first cracking, larger amounts of liquid Zn or Zn vapor can fill the initial crack and induce further cracking.

From the results obtained, we can derive a simple model of the processes occurring during the initial stage of Zn metal embrittlement in a PHS steel:

1. During annealing above 870 °C, the following phases are formed from bulk to surface: γ -Fe, α -Fe(Zn), liquid Zn/Fe, and solid Zn-oxides (see Figures 2 and 6).
2. The Zn and Fe interdiffusion triggers the growth of α -Fe(Zn), which separates the liquid Zn from the steel base. The growth is mainly determined by the α -Fe(Zn) Zn-Fe reaction and bulk diffusion, respectively. GB diffusion is smeared out quickly by the high solubility of Zn in the α -Fe(Zn).
3. Different diffusion constants and solubilities of the alloy elements in α -Fe(Zn) and γ -Fe lead to an additional region between the α -Fe(Zn) and the base steel. In our experiments, this region transforms later during quenching into Zn-free ferrite, forming an almost continuous layer along the interface of the steel and the coating.
4. Only at positions where the α -Fe(Zn) Zn-Fe reaction is hampered by stabilized austenite can fast diffusion along austenite GBs happen. We assume a generally much slower bulk diffusion of Zn in austenite compared with ferrite. This leads to several μm deep penetrations of Zn with a low concentration along these specific GBs (see Figures 8–10) during annealing above austenitizing temperature.
5. During forming, when a force is applied, cracks are formed in the Zn coating at the position of the Zn-weakened PAGB and expose these Zn-sensitive GBs.

6. Present liquid Zn or Zn vapor covers the new surfaces and can further trigger MIE, and macroscopic cracks are formed along these PAGBs (see Figure 3).
7. This process can continue during hot forming in the presence of Zn until the hardening and the austenite–martensite transformation take place.
8. The still-present liquid Zn or Zn vapor accumulates in the microcrack tip via the capillary effect (see Figures 4 and 5) and can form additional Fe–Zn phases.

5. Conclusions

We investigated MIE and its underlying mechanisms using a detailed microstructure characterization on two different samples of the same 20MnB8 steel. The first sample was hot-dip galvanized, hot-formed, and press-hardened. Using AES, SEM-EDX, and STEM-EDX, we found wedge-shaped Zn containing phases smaller than 100 nm at the crack tips. These findings demonstrate the importance of a Zn source for MIE crack propagation at prior austenite grain boundaries.

On the second samples, which were electrogalvanized featuring the same thermal history but without deformation, we could detect Zn-wetting of prior austenite grain boundaries. Under ultra-high vacuum conditions of an AES, Zn could be detected down to a depth of 25 μm below the $\alpha\text{-Fe(Zn)}$ phases on in situ-cracked PAGBs. The amount of Zn in the grain boundaries was estimated to be in the order of a monolayer Zn or less. We could additionally show that a low amount of Zn can wet austenite GBs during austenitizing annealing several tens of μm deep into the base steel matrix with STEM-EDX.

We believe that austenite GB wetting happens at a position where the $\alpha\text{-Fe(Zn)}$ -ferrite reaction is suppressed and $\gamma\text{-Fe(Zn)}$ can be formed. The Mn distribution, together with the C distribution (which is unfortunately not measurable with STEM-EDX), is thought to be the major reason for the suppression of $\alpha\text{-Fe(Zn)}$ formation. The contribution of Zn-weakened PAGBs to the quantity of microcrack formation is still up for debate. The dominant mechanism for microcrack formation on the steel surface during hot forming is the origination of cracks in the Zn coating. However, weakened PAGB should play an important role in the further propagation into the steel matrix.

Supplementary Materials: The following supporting information can be downloaded at: <https://www.mdpi.com/article/10.3390/met14010046/s1>. Figure S1. This figure illustrates the atom probe tomography (APT) liftout procedure and how composition profile graphs were obtained from multiple APT measurements. (a) shows a large-scale EBSD mapping of the interface region between Zn coating (top) and martensitic base steel (bottom). A band contrast (BC) image (top), as well as an inverse pole figure (IPF) map (bottom) are shown in (a). The projection axis for the IPF map is perpendicular to the steel/coating interface (i.e., y-direction). Such mappings were used to screen a large number of potential grain boundaries and identify suitable ones for an APT liftout. We targeted grain boundaries that lead straight into the martensite so that we would be able to follow the GB into the martensitic microstructure and contain a GB within the APT tip (i.e., we targeted the arrangement shown in Figure 8b where the Zn containing $\alpha\text{-Fe(Zn)}$ directly touches the martensite without the occurrence of the Zn-free ferrite). Two GBs along which we performed a liftout are marked by orange and cyan arrows. (b,d) show the grain boundary that was lifted out for liftout number one (orange highlighting color) at different magnifications in backscattered electron (BSE) micrographs as well as the corresponding zoom to the IPF EBSD mapping, (c,e) show the grain boundary of liftout number two (cyan highlighting color). (d,e) mark the positions of the individual APT tips that were produced from the liftout. Each cross represents an individual APT tip, hence an individual APT measurement that yields a chemical composition at the position of the cross. The results of the chemical composition analysis are shown in the form of a graph in Figures S3 and S4. and in tabular form in Tables S1 and S2f) shows a few snapshots of the liftout procedure performed: first a promising GB is identified. A rectangular region around the GB is covered with a protective Pt deposit to preserve the GB during the subsequent FIB milling. Material is removed adjacent and underneath the Pt deposit using FIB milling. The remaining wedge-shaped material is lifted out using a micromanipulator, chopped into individual segments (here 6 segments) which are placed on Si posts and sharpened into needle shaped APT tips by annular FIB milling. Figure S2. EDX mapping of the boundary

lifted out for the APT measurement set number one at different magnifications. (a) covers a larger area of the Zn coating region. (b) is a magnified view of the liftout region. Mappings using both L and K line are shown for Zn. K lines are used for all other elements. The electron micrograph was acquired using backscattered electrons (BSE). Different features are discernable in the elemental mappings: α -Fe(Zn) at the top, a band of Γ -phase in the region of α -Fe(Zn), the martensitic base steel at the bottom and Si-Mn-oxides inside the Γ -phase. These Si-Mn-oxide particles seem also slightly enriched in Al. There appear to be some Mn-rich particles in the martensitic base steel, but it seems that the resolution of the SEM-EDX mapping here is not sufficient to clearly resolve them. (c) shows an overlay of the BSE micrograph with the Zn EDX signal clearly demonstrating the layer of Zn-free ferrite separating the martensitic base steel from the Zn-rich ferrite (α -Fe(Zn) phase). (d,e) depict two additional examples Zn EDS mappings overlaid with BSE micrographs. Figure S3. Composition profiles along the Zn coating into the martensitic base steel (from left to right). (a) shows the chemical composition of the 6 APT measurements from liftout number one (see Figures S1 and S2). The electron micrograph underneath the graph is aligned in such way that the markings of the APT tip positions on the micrograph are aligned with the data points in the graph. Already from the micrograph it is apparent that the first APT measurement (letter a) is placed inside the Γ -phase, the next three APT measurements (letters b–d) are located inside α -Fe(Zn) while the last two measurements (letters e and f) are in the martensitic base steel. (b) is the same as (a) but for liftout number two. Unfortunately, two APT tips (letters b and d) fractured prematurely, which is why the corresponding data points in the graph are missing. Here only APT tip f is located in the martensitic base steel, all other APT tips are within the α -Fe(Zn) phase. The results of liftout number two are shown here, to demonstrate the reproducibility of the results obtained despite the small volume analyzed in each individual APT measurement. The same gradient of decreasing Zn concentration and increasing Mn, Si and Cr gradient moving towards the base steel is found in both sets of measurements. The C composition of the martensite is higher than the nominal composition of approximately 1 at% in both measurements in liftout one as well as the single measurement in this region in liftout two, which could be an enrichment of C during the α -Fe(Zn) formation on the steel base side due to a low solubility in the formed phase. Other reasons could be due to local variations in C concentration, as well as C contaminations during any of the preparation steps. Table S1. Composition of the individual APT measurements from liftouts number one corresponding to the graph shown in Figure S3a). Table S2. Composition of the individual APT measurements from liftout number two corresponding to the graph shown in Figure S3b). Note that the measurements b and d from this liftout did not yield a result since the APT tips fractured prematurely. Figure S4. APT analysis of segregation to grain boundaries and dislocations. The top of this figure shows so-called atom maps (i.e., all C atoms in a thin slice through the dataset) of two different measurements in the martensitic region. A GB is marked by cyan arrows, some dislocations are marked by orange arrows. (b) corresponds to the composition profile through the boundary marked by cyan arrows in (a). The composition profile was calculated along a cylinder of 20 nm diameter across a straight segment of the boundary. Note that the Zn composition in (b) is higher than the aforementioned 0.002 at% which is due to the fact, that the Zn composition given for the martensitic matrix was corrected for the background, but for the graph we decided to show the uncorrected values together with the background (BG) in the graph. The BG was determined separately for each composition profile. (c–e) show profiles through different dislocation from the APT dataset in (a). (g,h) show profiles through two different dislocations from the APT dataset in (d). The atom map shown in (a) corresponds to the reconstruction of APT tip number 6 from liftout number 1. The graphs in (b,c,f,g) are extracted from this dataset. The atom map shown in (d) corresponds to the reconstruction of APT tip f from liftout number 2. The graphs shown in (e,h) are extracted from this dataset. It is apparent that the dislocations as well as the GB are marked by strong C enrichments. However, no other elements show any segregation tendency to the GB or dislocations. For the APT liftouts, we target grain boundaries in the α -Fe(Zn) that continued straight into the martensite and where no Zn-free ferrite section was present (see Figures S1 and S2). Unfortunately, we could not unambiguously identify a PAGB in the APT measurements. The GB marked by cyan arrows in (a) in the martensitic region is visible due to its C enrichment. However, no Zn segregation is present at this GB (as apparent in (b)). Due to missing crystallographic information, we cannot determine whether this GB is a PAGB which does not show any Zn wetting or if it is simply a random martensite boundary. We think that usually not all PAGBs are covered with Zn and due to the difficult pre-identification of potential Zn-wetted GBs, there is only a low probability of finding a Zn-wetted PAGB within APT tips with a limited number of attempts.

Author Contributions: M.A.: conceptualization, formal analysis, investigation, writing—original draft, and visualization; T.T.: investigation, writing—review and editing; P.K.: formal analysis, investigation, writing—review and editing, and visualization; J.D.: resources; K.H.: conceptualization and writing—review and editing; D.S.: resources and writing—review and editing; C.C.: formal analysis and investigation; J.H.: investigation; S.K.: conceptualization; J.F.: conceptualization, resources, writing—review and editing, and project administration; H.G.: conceptualization, validation, investigation, resources, data Curation, writing—original draft, visualization, supervision, project administration, and funding acquisition. All authors have read and agreed to the published version of the manuscript.

Funding: The financial support from the Austrian Federal Ministry of Labour and Economy, the National Foundation for Research, Technology and Development, and the Christian Doppler Research Association is gratefully acknowledged. J.D. and D.S. acknowledge the government of Upper Austria for financial support (project ASAES). Open Access Funding by the University of Linz.

Data Availability Statement: Data is contained within the article and Supplementary Material.

Acknowledgments: The authors are grateful to U. Tezins and A. Sturm for their support in the FIB and APT facilities at MPIE. Baptiste Gault is acknowledged for helpful discussions about APT data analysis.

Conflicts of Interest: Author M.A., C.C., J.H., S.K., J.F. was employed by the company Voestalpine Stahl GmbH. The remaining authors declare that the research was conducted in the absence of any commercial or financial relationships that could be construed as a potential conflict of interest.

References

- Karbasian, H.; Tekkaya, A.E. A review on hot stamping. *J. Mater. Process. Technol.* **2010**, *210*, 2103–2118. [[CrossRef](#)]
- Faderl, J.; Manzenreiter, T.; Radlmayr, M. Press hardening of hot-dip galvanized 22MnB5: A stable and reproducible process. In Proceedings of the 2nd International Conference on Hot Sheet Metal Forming of High-Performance Steel, Kassel, Germany, 15–17 June 2019; pp. 199–205.
- Bhattacharya, D.; Cho, L.; van der Aa, E.; Pichler, A.; Pottore, N.; Ghassemi-Armaki, H.; Findley, K.O.; Speer, J.G. Influence of the starting microstructure of an advanced high strength steel on the characteristics of Zn-Assisted liquid metal embrittlement. *Mater. Sci. Eng. A* **2021**, *804*, 140391. [[CrossRef](#)]
- Pant, P.; Rekha, M.Y.; Schubert, H.; Hilpert, B.; Brewer, L.N. Liquid metal embrittlement susceptibility of zinc-coated martensitic sheet steels. *Mater. Sci. Eng. A* **2023**, *863*, 143762. [[CrossRef](#)]
- Bhattacharya, D.; Cho, L.; Marshall, D.; Walker, M.; van der Aa, E.; Pichler, A.; Ghassemi-Armaki, H.; Findley, K.O.; Speer, J.G. Liquid metal embrittlement susceptibility of two Zn-Coated advanced high strength steels of similar strengths. *Mater. Sci. Eng. A* **2021**, *823*, 141569. [[CrossRef](#)]
- Prabitz, K.M.; Asadzadeh, M.Z.; Pichler, M.; Antretter, T.; Beal, C.; Schubert, H.; Hilpert, B.; Gruber, M.; Sierlinger, R.; Ecker, W. Liquid Metal Embrittlement of Advanced High Strength Steel: Experiments and Damage Modeling. *Materials* **2021**, *14*, 5451. [[CrossRef](#)] [[PubMed](#)]
- Bauer, K.-D.; Todorova, M.; Hingerl, K.; Neugebauer, J. A first principles investigation of zinc induced embrittlement at grain boundaries in bcc iron. *Acta Mater.* **2015**, *90*, 69–76. [[CrossRef](#)]
- Lynn, J.C.; Warke, W.R.; Gordon, P. Solid metal-induced embrittlement of steel. *Mater. Sci. Eng.* **1975**, *18*, 51–62. [[CrossRef](#)]
- Beckman, J.P.; Woodford, D.A. Gas phase embrittlement by metal vapors. *Metall. Trans. A* **1989**, *20*, 184–188. [[CrossRef](#)]
- Choi, D.-Y.; Sharma, A.; Uhm, S.-H.; Jung, J.P. Liquid metal embrittlement of resistance welded 1180 TRIP steel: Effect of electrode force on cracking behavior. *Met. Mater. Int.* **2019**, *25*, 219–228. [[CrossRef](#)]
- Takahashi, M.; Nakata, M.; Imai, K.; Kojima, N.; Otsuka, N. Liquid metal embrittlement of hot stamped galvanized boron steel sheet—Effect of heating time on crack formation. *ISIJ Int.* **2017**, *57*, 1094–1101. [[CrossRef](#)]
- Cho, L.; Kang, H.; Lee, C.; De Cooman, B.C. Microstructure of liquid metal embrittlement cracks on Zn-coated 22MnB5 press-hardened steel. *Scr. Mater.* **2014**, *90–91*, 25–28. [[CrossRef](#)]
- Kang, H.; Cho, L.; Lee, C.; De Cooman, B.C. Zn penetration in liquid metal embrittled TWIP steel. *Metall. Mater. Trans. A* **2016**, *47*, 2885–2905. [[CrossRef](#)]
- Lee, C.W.; Fan, D.W.; Sohn, I.R.; Lee, S.-J.; De Cooman, B.C. Liquid-metal-induced embrittlement of Zn-coated hot stamping steel. *Metall. Mater. Trans. A* **2012**, *43*, 5122–5127. [[CrossRef](#)]
- Lee, C.W.; Choi, W.S.; Cho, L.; Cho, Y.R.; De Cooman, B.C. Liquid-metal-induced embrittlement related microcrack propagation on Zn-coated press hardening steel. *ISIJ Int.* **2015**, *55*, 264–271. [[CrossRef](#)]
- Beal, C.; Kleber, X.; Fabregue, D.; Bouzekri, M. Embrittlement of a zinc coated high manganese TWIP steel. *Mater. Sci. Eng. A* **2012**, *543*, 76–83. [[CrossRef](#)]
- Jung, G.; Woo, I.S.; Suh, D.W.; Kim, S.J. Liquid Zn assisted embrittlement of advanced high strength steels with different microstructures. *Met. Mater. Int.* **2016**, *22*, 187–195. [[CrossRef](#)]

18. Maleki, K.; McDermid, J.R.; McNally, E.A.; Bassim, N.D. On the origin of micro-cracking in in Zinc-coated press hardened steels. In Proceedings of the 12th International Conference on Zinc & Zinc Alloy Coated Steel Sheet—GALVATECH 2021, Virtual Conference, 21–23 June 2021; pp. 1086–1095.
19. Razmpoosh, M.H.; DiGiovanni, C.; Zhou, Y.N.; Biro, E. Pathway to understand liquid metal embrittlement (LME) in Fe-Zn couple: From fundamentals toward application. *Prog. Mater. Sci.* **2021**, *121*, 100798. [[CrossRef](#)]
20. Ikeda, Y.; Yuan, R.; Chakraborty, A.; Ghassemi-Armaki, H.; Zuo, J.M.; Maaß, R. Early stages of liquid-metal embrittlement in an advanced high-strength steel. *Mater. Today Adv.* **2022**, *13*, 100196. [[CrossRef](#)]
21. Li, J.; Tong, C.; Zhang, R.; Shi, Z.; Lin, J. A data-informed review of scientific and technological developments and future trends in hot stamping. *Int. J. Lightweight Mater. Manuf.* **2023**, *in press*. [[CrossRef](#)]
22. Razmpoosh, M.H.; Langelier, B.; Marzbanrad, E.; Zurob, H.S.; Zhou, N.; Biro, E. Atomic-scale Investigation of Liquid-Metal-Embrittlement Crack-path: Revealing Mechanism and Role of Grain Boundary Chemistry. *Acta Mater.* **2021**, *204*, 116519. [[CrossRef](#)]
23. Ma, Z.; Peng, W.; Ding, C.; Wu, G.; Zhang, J. Study on Cracking Behavior of High-Strength Steels by Liquid Zinc-Induced Embrittlement. *Steel Res. Int.* **2022**, *93*, 2100483. [[CrossRef](#)]
24. Kolnberger, S.; Haslmayr, J. Method and Device for Producing Hardened Steel Components. Justia Patent 20190047032, 14 February 2019.
25. Haslmayr, J.; Kolnberger, S.; Schwinghammer, H.; Sommer, A.; Tutewohl, B. Method and Device for Producing Hardened Steel Components. Justia Patent 20190048432, 14 February 2019.
26. Kolnberger, S.; Faderl, J.; Kurz, T.; Haslmayr, J. Avoiding Zinc induced cracking in hot forming. In Proceedings of the 12th International Conference on Zinc & Zinc Alloy Coated Steel Sheet—GALVATECH 2021, Virtual Conference, 21–23 June 2021; pp. 1059–1068.
27. Ling, Z.; Wang, M.; Kong, L. Liquid metal embrittlement of galvanized steels during industrial processing: A review. In *Transactions on Intelligent Welding Manufacturing*; Chen, S., Zhang, Y., Feng, Z., Eds.; Springer: Singapore, 2018; pp. 25–42.
28. Johansson, A.; Ljung, H.; Westman, S. X-ray and neutron diffraction studies on gamma-Ni, Zn and gamma-Fe, Zn. *Acta Chem. Scand.* **1968**, *22*, 2743–2753. [[CrossRef](#)]
29. Koster, A.S.; Schoone, J.C. Structure of the cubic iron–zinc phase Fe₂₂Zn₇₈. *Acta Crystallogr. B* **1981**, *37*, 1905–1907. [[CrossRef](#)]
30. Belin, C.H.E.; Belin, R.C.H. Synthesis and crystal structure determinations in the Γ and δ phase domains of the iron–zinc system: Electronic and bonding analysis of Fe₁₃Zn₃₉ and FeZn₁₀, a subtle deviation from the Hume–Rothery standard? *J. Solid State Chem.* **2000**, *151*, 85–95. [[CrossRef](#)]
31. Brown, P.J. The structure of the δ -phase in the transition metal–zinc alloy systems. *Acta Crystallogr.* **1962**, *15*, 608–612. [[CrossRef](#)]
32. Janik, V.; Lan, Y.; Beentjes, P.; Norman, D.; Hensen, G.; Sridhar, S. Zn Diffusion and α -Fe(Zn) Layer Growth During Annealing of Zn-Coated B Steel. *Metall. Mater. Trans. A* **2016**, *47*, 400–411. [[CrossRef](#)]
33. Järvinen, H.; Honkanen, M.; Patnamsetty, M.; Järn, S.; Heinonen, E.; Jiang, H.; Peura, P. Press hardening of zinc-coated boron steels: Role of steel composition in the development of phase structures within coating and interface regions. *Surf. Coat. Technol.* **2018**, *352*, 378–391. [[CrossRef](#)]
34. Kitahara, H.; Ueji, R.; Tsuji, N.; Minamino, Y. Crystallographic features of lath martensite in low-carbon steel. *Acta Mater.* **2006**, *54*, 1279–1288. [[CrossRef](#)]
35. Gourgues, A.-F.; Flower, H.M.; Lindley, T.C. Electron backscattering diffraction study of acicular ferrite, bainite, and martensite steel microstructures. *Mater. Sci. Technol.* **2000**, *16*, 26–40. [[CrossRef](#)]
36. Bhattacharya, D.; Cho, L.; Colburn, J.; Smith, D.; Marshall, D.; van der Aa, E.; Pichler, A.; Ghassemi-Armaki, H.; Pottore, N.; Findley, K.O.; et al. Influence of selected alloying variations on liquid metal embrittlement susceptibility of quenched and partitioned steels. *Mater. Des.* **2022**, *224*, 111356. [[CrossRef](#)]
37. Feliu, S., Jr.; Barranco, V. XPS study of the surface chemistry of conventional hot-dip galvanised pure Zn, galvanneal and Zn-Al alloy coatings on steel. *Acta Mater.* **2003**, *51*, 5413–5424. [[CrossRef](#)]
38. Allegra, L.; Hart, R.G.; Townsend, H.E. Intergranular zinc embrittlement and its inhibition by phosphorus in 55 pct Al-Zn-coated steel sheet. *Metall. Mater. Trans. A* **1983**, *14*, 401–411. [[CrossRef](#)]
39. Luo, J.; Cheng, H.; Asl, K.M.; Kiely, C.J.; Harmer, M.P. The role of a bilayer interfacial phase on liquid metal embrittlement. *Science* **2011**, *333*, 1730–1733. [[CrossRef](#)] [[PubMed](#)]

Disclaimer/Publisher’s Note: The statements, opinions and data contained in all publications are solely those of the individual author(s) and contributor(s) and not of MDPI and/or the editor(s). MDPI and/or the editor(s) disclaim responsibility for any injury to people or property resulting from any ideas, methods, instructions or products referred to in the content.